Understanding the charge storage mechanism to achieve high capacity and fast ion storage in sodium-ion capacitor anodes by using electrospun nitrogen-doped carbon fibers

Understanding the charge storage mechanism to achieve high capacity and fast ion storage in sodium-ion capacitor anodes by using electrospun nitrogen-doped carbon fibers

*Runyu Yan, Elinor Josef, Haijian Huang, Karen Leus, Markus Niederberger, Jan P. Hofmann, Ralf Walczak, Markus Antonietti, Martin Oschatz**

R. Yan, Dr. E. Josef, R. Walczak, Prof. Dr. M. Antonietti, Dr. M. Oschatz,
Department of Colloid Chemistry, Max Planck Institute of Colloids and Interfaces, Am Mühlenberg 1, 14476 Potsdam (Germany).
E-mail: martin.oschatz@mpikg.mpg.de

H. Huang, Prof. Dr. M. Niederberger
Laboratory for Multifunctional Materials, Department of Materials, ETH Zürich, Vladimir-Prelog-Weg 5, 8093 Zürich (Switzerland).

Prof. Dr. K. Leus
Department of Chemistry, Ghent University, Krijgslaan 281, S3, 9000 Gent (Belgium).

Dr. J. P. Hofmann
Laboratory for Inorganic Materials and Catalysis, Department of Chemical Engineering and Chemistry, Eindhoven University of Technology, Groene Loper 5, 5612 AE, Eindhoven (The Netherlands).

Abstract

Nitrogen-rich carbon fibers (HAT-CNFs) are produced by electrospinning a mixture of hexaazatriphenylene-hexacarbonitrile (HAT-CN) with polyvinylpyrrolidone and subsequent thermal condensation. HAT-CNFs show nitrogen contents of up to 15 wt% and a microporous nanostructure. Bonding motives, electronic structure, and content of nitrogen heteroatoms, porosity, and degree of carbon stacking can be controlled by the condensation temperature due to the use of the HAT-CN with predefined nitrogen binding motives. The materials show remarkable reversible capacities (395 mAh g^{-1} at 0.1 A g^{-1}) and rate capabilities (106 mAh g^{-1} at 10 A g^{-1}) as anode material for sodium storage, resulting from the abundant heteroatoms, enhanced electrical conductivity, and rapid charge carrier transport in the one-dimensional nanoporous structure of the fibers. HAT-CNFs also serve as a series

of model compounds for the investigation of the contribution of sodium storage by intercalation and reversible binding on nitrogen sites at different rates. There is an increasing contribution of intercalation to the charge storage with increasing condensation temperature which becomes less active at high rates. A hybrid sodium ion capacitor full cell combining HAT-CNF as the anode and salt-templated porous carbon as the cathode provides remarkable energy and power density in the voltage range of 0.5-4.0 V (95 Wh kg^{-1} at 0.19 kW kg^{-1}, and still maintains 18 Wh kg^{-1} at 13 kW kg^{-1}).

Introduction

The significance of storing electricity for the functioning of our society has been revealed by science and industry in recent decades. Electrochemical energy storage devices play a vital role and electrochemical capacitors (ECs) are a key element in that context. However, the inferior energy density of ECs remains a major challenge.[1]

Hybrid ion capacitors (HICs), including Li-ion capacitors (LICs) and Na-ion capacitors (NICs) can be a step forward to tackle this problem. HICs contain a high-energy battery-type anode and a high-power capacitive-type cathode.[2] From the mechanistic point of view, charges are simultaneously stored in the HIC by anion adsorption on the capacitive-type cathode surface and via Faradaic cation intercalation/reaction in the battery-type anode, respectively.[3] Combining the working mechanisms of high power ECs and high energy batteries, HICs provide the possibility to combine their individual advantages. Moreover, the charge-discharge processes of these two electrodes are performed in different potential ranges (the anode at high negative working potentials where alkali metals are strong and the supercapacitor cathode at high positive potentials which are usually not accessible to battery set-ups), thus enlarging the operating voltage window, which is among the most efficient methods to enhance the energy density.[4] In contrast to LICs, NICs do not suffer from the limited abundance of lithium but due to the larger weight and size of sodium ions, their storage is usually encountered with inferior capacity and rate capability. The biggest obstacle in the development of high-performance

NICs is the kinetic imbalance between the cathode and anode. The physical ion adsorption on the cathode (usually nanoporous carbon) surface is much faster than the chemical reactions in the anode. This causes intensive efforts to develop Faradaic anodes with sufficient dynamics to match the non-Faradaic cathode.

Promising candidates for anode materials include various carbonaceous materials,[5] metal/alloys,[6] metal oxides,[7] and metal sulfides.[8] Among them, carbon materials have attracted considerable attention due to their high storage capacity for sodium, high electrical conductivity, abundant resources, excellent stability, and low cost.[9] Great efforts have been devoted to tailoring the atomic construction and porosity of carbons[10] which can contribute to sodium storage and promote rapid ion transport, thus facilitating the rate capability of the anodes. Among the various morphologies, electrospun carbon fibers have received particular attention due to their potential scalability and enhanced electrochemical performance as NIC anodes.[11] The latter is mainly due to their one-dimensional nanostructure with abundant interconnections between the fibers which facilitates electrical conductivity and ion transport, pushing forward the capacity beyond 300 mA h g^{-1}.[11a, 12] Another promising approach is the introduction of heteroatoms, especially nitrogen, to provide additional charge storage capacity through reversible binding of sodium to the nitrogen-based functional groups.[5a] The nitrogen content in these nitrogen-doped carbons is normally limited[12-13] but higher nitrogen content could further enhance the sodium storage capacity as, for example, carbon nitride has proved its extraordinary lithium capacity (933 mAh g^{-1}).[14] Although this combination of high heteroatom content and one-dimensional nanostructure is quite promising for NIC anodes, the synthetic approaches for such materials are still limited.

In addition to the development of advanced materials for NIC anodes, the mechanism of sodium storage in carbon materials is still not completely understood. The main contributions for storage capacity originate from the underpotential deposition on the high energy adsorption sites on the carbon electrode surface such as defective sites and functional groups as well as from the intercalation into

the stacked graphene layers of the carbons. Although still debated, most studies indicate that the slope region at higher voltage during discharge corresponds to adsorption of sodium while the capacity in the low voltage range corresponds to intercalation.[15] For sure, there is still a lack of systematic studies and comprehensive interpretation of the mechanism of sodium storage in carbon (and especially in nitrogen-doped carbon) materials. Beyond these questions related to the fundamental storage mechanism as such, there remains also a lack of profound understanding about the influence of and the interplay between electrode properties such as heteroatom content, nanostructure/porosity of the electrode, electrical conductivity, and degree of graphitization on the capacity and rate capability of NICs. It is generally believed that nitrogen-doping has a positive impact on the sodium storage performance of carbon materials but illuminating these structure-performance relationships in detail requires systematic studies. It is the major scope of this work to investigate these structure-performance relationships by utilizing a series of model carbon materials with varying electron density distribution, nitrogen content, nitrogen binding motives, morphology, and porosity.

In this study, we use hexaazatriphenylene-hexacarbonitrile (HAT-CN) and polyvinylpyrrolidone (PVP) as precursors to electrospin a free-standing carbon fiber composite (nitrogen-doped carbon and partially graphitic carbon) film with nitrogen contents up to 15 wt%. The free-standing fibers present remarkable performance as anodes for NICs, with a reversible capacity of 395 mAh g^{-1} at 0.1 A g^{-1} and high rate capacity retention of 106 mAh g^{-1} at 10 A g^{-1}. These properties are ascribed to the high electrical conductivity and efficient ion transport introduced by the interconnected one dimensional structure of the fibers, and the high nitrogen content introduced by condensation of HAT-CN. Furthermore, the mechanism of sodium storage in this material is illuminated by adjusting the ratio of nitrogen-doped carbon and graphitic carbon domains through different condensation temperatures. The intercalation process takes place only in the low underpotential range, while we attribute the sodium storage in the high underpotential range to adsorption on the nitrogen functional groups, which dominantly contribute to the high capacity, in particular at low scan rates. A NIC full cell with HAT-

CNF as the anode and highly porous salt-templated carbon (STC) is then set-up to quantify the behavior of the two storage materials. Throughout data analysis we focus on mechanistic findings in terms of the sodium storage contributions to capacity as well as the importance of the one-dimensional nanostructure and the electrical conductivity for rate capability.

Results and Discussion

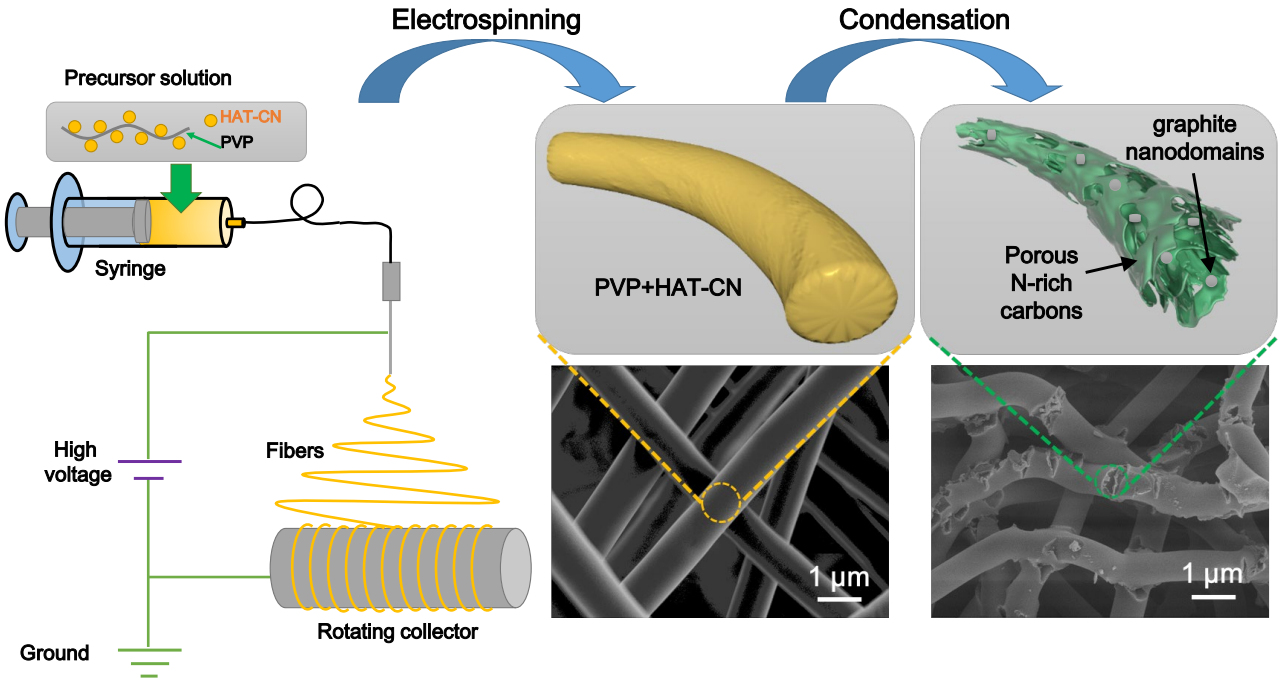

Scheme 1. Preparation of the porous HAT-CNF by electrospinning and subsequent condensation.

A series of nitrogen-rich carbon fibers (denoted as HAT-CNFs) with different nitrogen content was prepared by electrospinning employing HAT-CN mixed with the matrix polymer polyvinylpyrrolidone (PVP) as the precursors. Thermal condensation of this mixture results in a large volume of structural microporosity and high pyrazinic nitrogen content introduced by the molecular structure of HAT, while PVP is employed as a processing aid for electrospinning. HAT-CN was synthesized according to a previously described procedure[16] and dissolved in dimethylformamide (DMF) together with PVP. The precursor solution was electrospun into a fiber matrix composed of PVP and HAT-CN (**Scheme 1**). The HAT-CNF-700, HAT-CNF-850, and HAT-CNF-1000 were obtained by condensation of the precursor fibers under N_2 atmosphere for 1 h at 700, 850, and 1000 °C, respectively. Thermal

decomposition of PVP and condensation of HAT-CN lead to gas evolution and to the generation of roughness on the surface of the fibers (**Scheme 1**). Thermogravimetric analysis (TGA) under N_2 (**Figure S1**) indicates that the residual mass of the fiber precursors is significantly higher than that of the pure HAT-CN, suggesting that HAT-CNFs contain excess carbon (likely also slightly nitrogen-doped) derived from PVP in addition to the very nitrogen-rich product of HAT-CN condensation. This explains the lower nitrogen content of HAT-CNFs compared with that of the carbon derived from pure HAT-CN (HAT-850) at the same calcination temperature (**Table 1**). Elemental analysis shows that the nitrogen contents of HAT-CNF-700, HAT-CNF-850, HAT-CNF-1000 still reaches values as high as 15 wt%, 10 wt%, and 5 wt%, respectively (**Table 1**). Thus, from the molecular point of view, HAT-CNFs can be described as nitrogen-doped carbon materials, in which the nitrogen-doped sites can possibly act as the active sites to adsorb sodium ions for the improved capacity, while the additional carbon (mostly derived from PVP) enhances the electrical conductivity.

Table 1. Specific surface area (SSA), total pore volume (V_t), nitrogen content of the carbon materials determined by elemental analysis (EA), SEM-EDX, and XPS, as well as I_D/I_G ratio and full width at half maximum (FWHM) of the D-band obtained by Raman spectroscopy of the HAT-CNF materials prepared at different temperatures and the non-spun HAT-850 reference sample.

Sample name	SSA (m^2/g)	V_t (cm^3/g)	Nitrogen content (EA wt%)	Nitrogen content (EDX wt%)	Nitrogen content (XPS wt%)	I_D/I_G	FWHM of D band (cm^{-1})
HAT-CNF-700	308	0.12	15	19	15	1.1	181.2
HAT-CNF-850	337	0.18	10	13	9	1.1	180.2
HAT-CNF-1000	644	0.27	5	6	4	1.0	175.8
HAT-850	642	0.28	17	20	/	/	/

The carbonized fibers have a high aspect ratio and are continuous with a narrow diameter distribution as shown in the scanning electron microscopy (SEM) images (**Figure 1a-c**). The diameter of the fibers decreases with the increase of the condensation temperature to ~1000 nm, 800 nm, and 400 nm for

HAT-CNF-700, HAT-CNF-850, and HAT-CNF-1000, respectively (**Figure 1d-e**), i.e. the mass loss and the density increase are taken up by lateral shrinking. Regardless of the condensation temperature, the carbon fibers exhibit an intact one-dimensional nanostructure with abundant surface defects. This wire-like morphology is useful to provide low electric resistance, while the interstitial mesh openings enable unrestricted ion transport inside the materials at the same time. The scanning electron microscopy energy dispersive X-ray spectroscopy (SEM-EDX) mapping images (insets in **Figure 1a-c**) reveal the uniform distribution of carbon and nitrogen within the fibrous framework. In agreement with the results from elemental analysis, the increase of calcination temperature results in a gradual decrease of nitrogen content (**Table 1**).

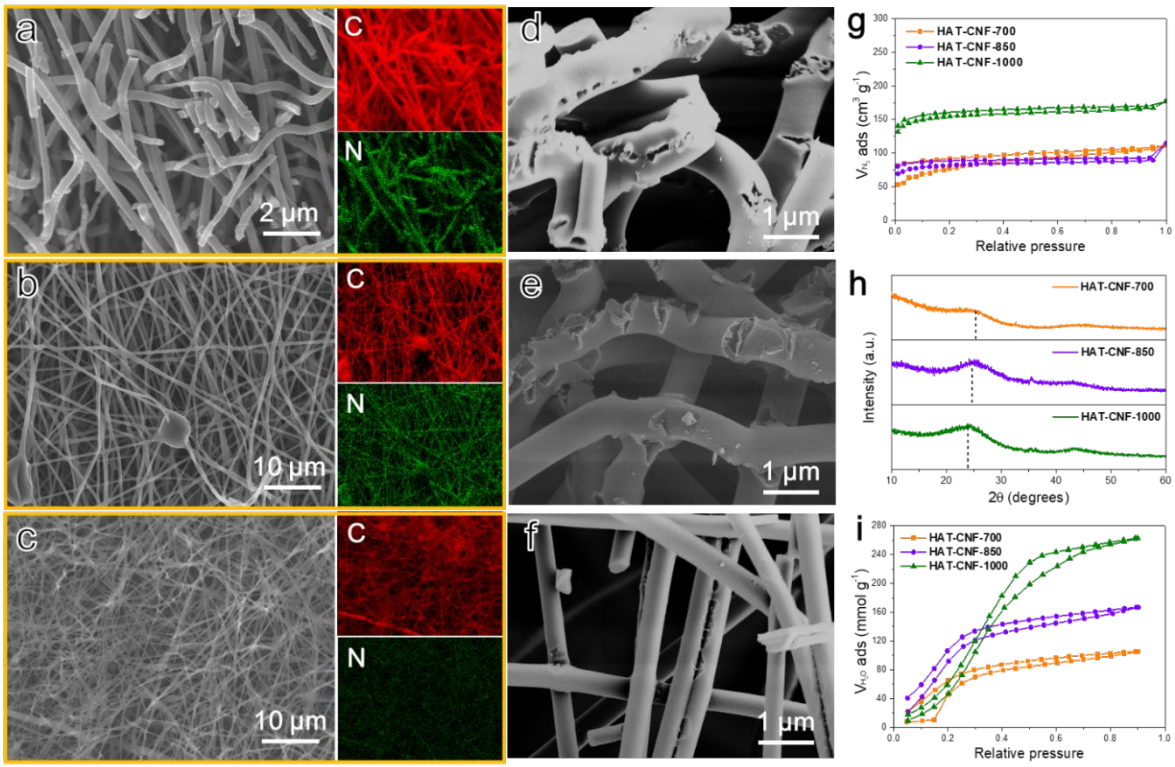

Figure 1. SEM images and EDX mapping (C and N) of (a) HAT-CNF-700, (b) HAT-CNF-850, and (c) HAT-CNF-1000. SEM images of (d) HAT-CNF-700, (e) HAT-CNF-850, and (f) HAT-CNF-1000 at higher magnification. (g) N_2 physisorption isotherms (at -196 °C) of HAT-CNFs. (h) XRD patterns of HAT-CNFs. (i) Water vapor physisorption isotherms (at 25 °C) of HAT-CNFs.

N_2 physisorption experiments at -196 °C were carried out to analyze the pore structure (**Figure 1g**, and **Table 1**). All the samples show type I(b) isotherms indicating the presence of a small amount of narrow

mesopores in addition to the abundant structural micropores.[17] The specific surface area (SSA) and the pore size distribution (PSD) were analyzed by employing the quenched-solid density functional theory (QSDFT) for N_2 adsorbed on carbon with slit/cylindrical pore shape.[18] HAT-CNF-700 shows a moderate internal DFT SSA of 308 $m^2 g^{-1}$. With the increase of the temperature, the internal SSAs gradually increase to 337 $m^2 g^{-1}$ and 644 $m^2 g^{-1}$ for HAT-CNF-850 and HAT-CNF-1000, respectively (**Table 1**). The total pore volume inside the fibers exhibits the same trend, rising from 0.12 $cm^3 g^{-1}$ for HAT-CNF-700, to 0.18 $cm^3 g^{-1}$ for HAT-CNF-850, followed by 0.27 $cm^3 g^{-1}$ for HAT-CNF-1000. All those values are to be considered as low, not geometrically interrupting the electron conductivity in those materials. The PSDs also confirm their mainly microporous structure and small volumes of narrow mesopores of ~3 nm in diameter (**Figure S2**). The porous structure was additionally investigated by transmission electron microscopy (TEM) imaging (**Figure S3**), which shows the typical appearance of porous carbon materials in accordance with the N_2 physisorption isotherms. X-ray diffraction (XRD) results (**Figure 1h**) of all the samples showed only broad (002) and (101) carbon peaks at ~26° and ~44° 2Theta, verifying their mainly weakly ordered structure as it is typical for porous carbon materials.[19] An increase of the condensation temperature results in more pronounced peaks with higher intensity, indicating the higher extent of graphitic stacking. It is also worth noting that the (002) carbon peak is slightly shifted to lower angles with temperature increase (~26°, 25°, and 24° for HAT-CNF-700, -850, and -1000, respectively), implying that the high temperature leads to expanded layer distance in the graphitic carbons, which facilitates sodium intercalation. Raman spectroscopy (**Figure S4**) is another useful tool to characterize sp^2-based carbon materials. The standard interpretation of Raman spectra as applied for pristine carbons cannot be strictly applied to N-doped carbons (as nitrogen doping introduces vibrational dissymmetry), but some interesting information about the carbon atomic structure can still be derived. In the Raman spectra, the similar peak height ratio of the D- (~1340 cm^{-1}, breathing mode of sp^2-carbon atoms in aromatic rings) and G-band (~1580 cm^{-1}, sp^2-carbon organized in chains or rings) (I_D/I_G in **Table 1**) suggests the

comparable degree of aromatization for all the samples. The broad D-bands in all samples reveal the existence of abundant disordered sections which are typical for amorphous carbons.[20] The slight decrease of FWHM with increasing temperature indicates the higher graphitization degree (**Figure S4** and **Table 1**). This is consistent with the XRD results.

X-ray photoelectron spectroscopy (XPS) was employed to characterize the electronic properties of the nitrogen atoms present in the HAT-CNFs (HAT-CNF-700, -850, and -1000). The nitrogen content of the three samples determined by XPS shows the same trend as that by EA and EDX (**Table 1**). In the high-resolution C 1s spectra (**Figure 2a-c**), the main peak at 284.6 eV can be assigned to the sp^2-hybridized carbons in carbon-carbon bonds. Its intensity increase at increasing temperature suggests the increasing graphitization degree which is consistent with the XRD and Raman spectroscopy results. The higher energy C 1s peak at 285.4 eV can be assigned to rather positively polarized sp^2 carbons bonded to nitrogen atoms. It is caused by the electronegativity difference between carbon (2.5) and nitrogen (3.0) atoms, forming a "C^+N^-" structure containing positively polarized carbon atoms because the electron density within the conjugated π-system is likely to shift to the more electronegative nitrogen atoms. This leads to the higher binding energy of the C 1s electrons in the positively polarized sp^2 carbons compared with that of carbon atoms bonded to other carbon atoms. The decrease of the nitrogen content in the HAT-CNFs is expected to decrease the amount of such positively polarized carbons, leading to the observed decay of this peak with increasing calcination temperature. The other C 1s peaks are associated with C=N bonding at 286.9 eV, C-N bonding at 288.4 eV, and N=C-N at 289.4 eV and could also correspond to a minor amount of carbon atoms bonded to oxygen.[21] They show a clearly declining trend with the drop of the nitrogen content. In contrast to the materials obtained at lower temperature, a significantly higher electric conductivity can be expected for HAT-CNF-1000 with rather electron-rich carbon atoms as well as less and more-positively polarized nitrogen atoms.

The high-resolution N 1s spectra (**Figure 2d-f**) of all HAT-CNFs can be fitted with three components. The peak at 402.8 eV is assigned to oxidized nitrogen.[22] The other two are relate to nitrogen species bonded to carbon atoms, including the negatively polarized nitrogen (pyrazinic N at ~398.5 eV) and positively polarized nitrogen (graphitic N at ~400.7 eV).[22] The binding energy of each peak slightly varies with the temperature changes. The peak position corresponding to the negatively polarized nitrogen changes from 398.4 eV in HAT-CNF-700 to 398.7 eV in HAT-CNF-1000 due to the higher electron density around the nitrogen atoms present after condensation at low temperature, which can increase the adsorption enthalpy of sodium on the nitrogen functional groups. The peak corresponding to more positively polarized nitrogen atoms also shifts slightly from 400.6 eV in HAT-CNF-700 to 400.7 eV in HAT-CNF-1000, illustrating the even more positive polarization of these nitrogen species after high condensation temperature treatment. With the temperature rise, the relative intensity (i.e. the height ratio of the ~398.5 eV peak and the ~400.6 eV peak) indicates a decreasing trend from 1.4 in HAT-CNF-700 to 0.7 in HAT-CNF-1000, further suggesting the presence of more negatively polarized nitrogen atoms after condensation at low temperature.

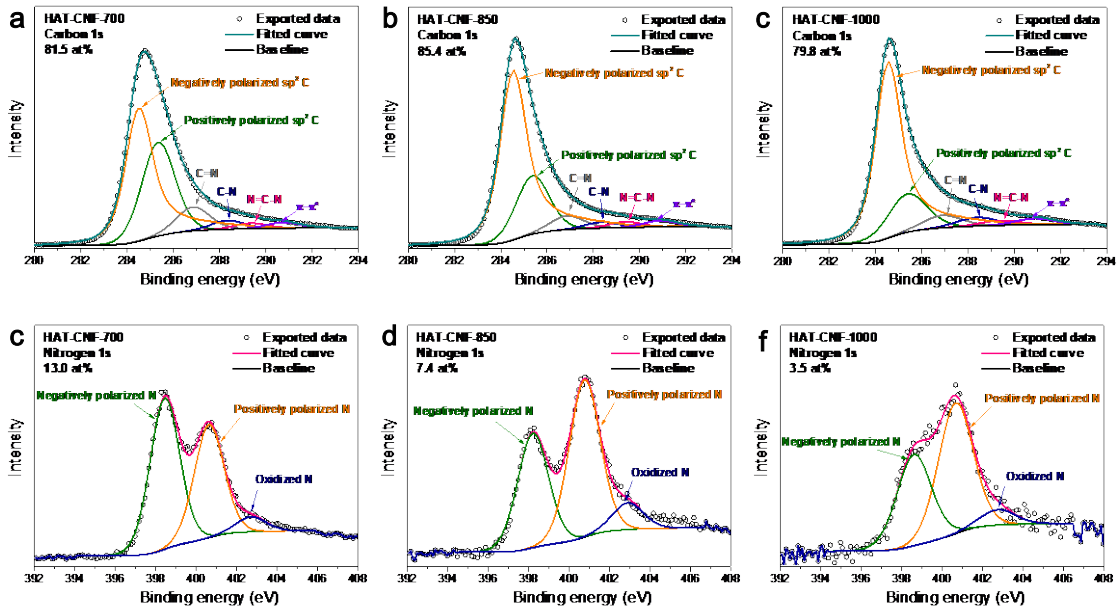

Figure 2. High-resolution XPS survey spectra of HAT-CNFs of (a-c) C 1s and (d-f) N 1s and their corresponding fitting curves.

Water vapor adsorption at 25 °C was measured to characterize the strength of interaction between the HAT-CNF samples and polar species such as water and sodium cations (**Figure 1i**). The total amount of adsorbed water shows the same trend as the total pore volume, i.e., the material with higher pore volume can adsorb a larger amount of water. On the other hand, there appears to be a big difference in the strength of water adsorption, which is related to the polarity of the materials. It can be seen that the slope of the adsorption branch below a relative pressure of 0.2 of the HAT-CNF-700 and -850 is apparently higher than that of the HAT-CNF-1000, indicating a higher enthalpy of water adsorption on the materials with higher nitrogen content prepared at low condensation temperature. That means that the water molecules have a stronger interaction with HAT-CNF-700 and HAT-CNF-850 than with HAT-CNF-1000. This is not only associated with their higher nitrogen content, as such but also attributed to the strongly polarized atomic structure built by positively polarized carbon atoms and negatively polarized nitrogen atoms which can specifically interact with the electronegative oxygen atoms and the electropositive nitrogen atoms present in water molecules, respectively. Based on these experiments, stronger interaction with sodium is expected for the samples prepared at lower condensation temperature. It is worth noting that the adsorption branch of HAT-CNF-700 shows a hysteresis starting from a relative pressure of ~0.15 with a subsequent drastic increase of absorbing amount. This might be explained by the pore blocking effects, where the rather narrow and small amount of micropores tend to resist the entering of the water molecules until this particular relative pressure.

HAT-CNFs were used as working electrodes for half-cell measurements in Swagelok-type test cells. Sodium foil and 1 M $NaClO_4$ in ethylene carbonate/propylene carbonate/fluoroethylene carbonate (45:45:10 by mass) were employed as the counter/reference electrode and electrolyte, respectively. The electrochemical performance of HAT-CNFs was first evaluated by galvanostatic charging/discharging process from 0.1 to 10 A g^{-1} between 0 and 2.5 V vs. Na/Na^+. At the low specific current of 0.1 A g^{-1}, the initial discharge capacity of HAT-CNF-700, -850, and -1000 is 875, 828, and

409 mAh g^{-1}, while the corresponding initial charge capacity decreases to 424, 381, and 218 mAh g^{-1} (**Figure 3a-c**), resulting from the typical irreversible processes in the initial cycles due to the formation of a solid-electrolyte interphase as well as the possible irreversible trapping and consumption of sodium.[5d, 23]

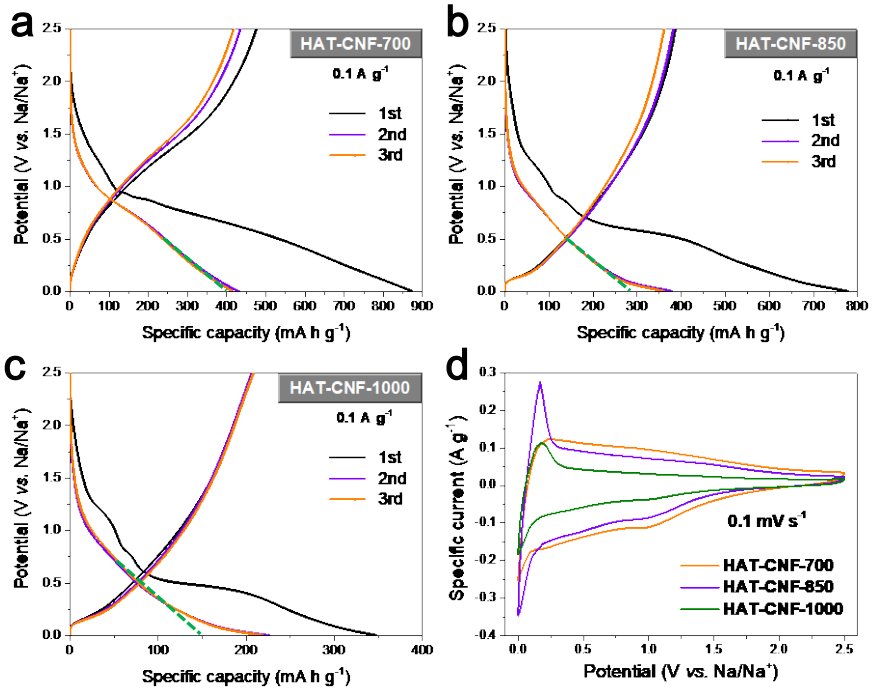

Figure 3. Anode sodium-storage half-cell tests of HAT-CNFs. Galvanostatic charge-discharge profiles of the first cycles of (a) HAT-CNF-700, (b) HAT-CNF-850, and (c) HAT-CNF-1000. (d) Cyclic voltammetry curves of HAT-CNFs scanned at the rate of 0.1 mV s^{-1}.

In the subsequent cycles, all the discharging curves show a very sharp slope region in the high underpotential range of 1.2-2.5 V, which likely corresponds to binding of sodium on specific well-stabilized sites on the porous and defect-rich HAT-CNF surface. When the potential decreases to 0.3-1.2 V, the slope of the curve decreases, and the capacity in this region depends about linearly on the nitrogen content (420, 298, and 146 mAh g^{-1} for the 15 wt%, 10 wt%, and 5 wt% nitrogen content, respectively, as revealed by the intercept of the green dashed line with the capacity axis in **Figure 3a-c**). The capacity in this range can be attributed to the reversible binding of sodium species on nitrogen-containing sites, which mainly originates from the nitrogen-doped carbon components in the fiber composite. The introduction of nitrogen sites obviously significantly increases the ability for

underpotential deposition or intercalation of sodium atoms onto special, highly ligating sites in the porous doped carbon. An underpotential difference of 1 V therein corresponds to an adsorption enthalpy of about 100 kJ mol^{-1} - a reasonable value for a polar atom as sodium. This corresponds to the enthalpy of evaporation of metallic sodium, i.e. the sodium interacts with these positions at least as strong as with its own counterparts. Similar effects are widely known from the field of gas adsorption where carbon materials with high heteroatom content show zeolite-like properties and rather strong adsorption enthalpies to polar molecules, which is here expressed in an electrochemical underpotential (according to the Nernst equation).[4b, 16c, 24] As zeolites are known for their strong interaction with alkali metal ions, it is not surprising that highly polar HAT-CNFs show high adsorption capacity for sodium. For example, the 420 mAh g^{-1} capacity of HAT-CNF-700 would translate to a sodium adsorption capacity of 15.7 $mmol_{Na}$ g^{-1} - a value that nicely compares to the water adsorption capacity of such materials.[16c, 25] Assuming an overall stoichiometry of HAT-CNF-700 of $C_{0.87}N_{0.13}$ (based on the elemental analysis data), the nitrogen content of ~10.6 $mmol_N$ g^{-1} is apparently closely related to the sodium storage capacity. Assuming that all the sloped capacity is due to binding of sodium near nitrogen, one nitrogen atom in HAT-CNF-550 relates to 1.5 sodium atoms. Interestingly, for HAT-CNF-850 ($C_{0.913}N_{0.087}$) and for HAT-CNF-1000 ($C_{0.957}N_{0.043}$) these values are still very close to 1.5, indicating that the sodium storage capacity in the slope region indeed precisely scales with the nitrogen content.

On the other hand, there are distinct differences in the low potential range. Typical plateaus are observed in the curves of HAT-CNF-850 and HAT-CNF-1000 at 0-0.3 V, while the curve of HAT-CNF-700 keeps a constant slope shape in this range. This is consistent with the increased degree of carbon layer stacking and the expanded inter-layer distance in the more graphitic carbons as revealed by the XRD data, which enables a possible intercalation of sodium ions. CV curves at the scan rate of 0.1 mV s^{-1} (**Figure 3d**) further confirm this interpretation. HAT-CNF-850 and -1000 exhibit pronounced peaks at around 0.2 V caused by the reversible intercalation/deintercalation of sodium ions,

while the rest of the curves is rather capacitive-type, representing the underpotential deposition of sodium species on specific binding sites. In summary, the mechanism of sodium storage in these nitrogen-rich HAT-CNF materials with partial graphitic stacking can be divided as follows. In the high and medium underpotential range, sodium is stored through deposition on low energy sites with high stabilization. In the low potential range, the intercalation of sodium ions into the carbon interlayers comes into play, which depends on the degree of graphitization and interlayer distance.

The reversible capacities at a specific current of 0.1 A g^{-1} of HAT-CNF-700, HAT-CNF-850, and HAT-CNF-1000 determined after 40 cycles are as high as 395 mAh g^{-1}, 361 mAh g^{-1}, and 209 mAh g^{-1}, respectively (**Figure 4d**). It is also worth noting that despite the highest SSA, HAT-CNF-1000 provides the lowest capacity, suggesting that the SSA and micropore volume have less influence on the sodium storage than nitrogen content.

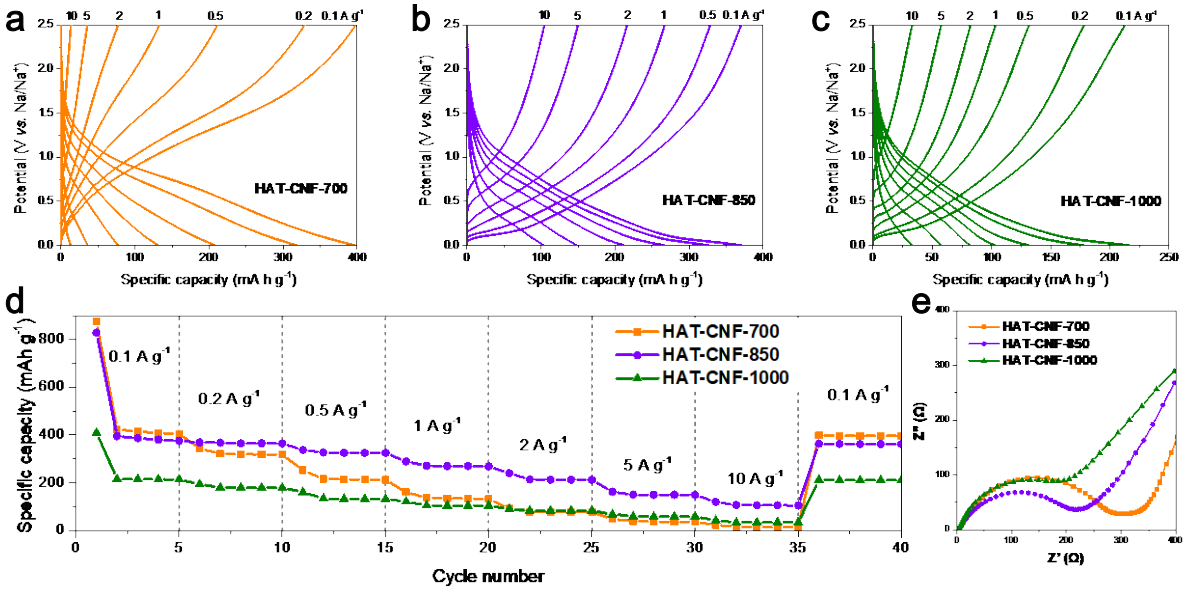

Figure 4. Half-cell tests of HAT-CNFs. Galvanostatic charge-discharge profiles at different specific currents of (a) HAT-CNF-700, (b) HAT-CNF-850, and (c) HAT-CNF-1000. (d) Rate performance of HAT-CNFs at different specific currents. (e) Nyquist plot of HAT-CNFs.

The rate capability was examined by varying the specific current in the range of 0.1 to 10 A g^{-1} (**Figure 4a-d**). All the samples show the typical decay of capacity with the increase of current, while the rate performance is related to the condensation temperature. At 10 A g^{-1}, the specific capacity of HAT-

CNF-700, -850, and -1000 is 13.6, 106, and 33.2 mAh g^{-1}, respectively, corresponding to retention of 3.4%, 29.3%, and 15.9%. The inferior rate capability of HAT-CNF-700 can be ascribed to the comparably low electrical conductivity (**Figure 4e**). The moderate rate capability of HAT-CNF-1000 is likely to be attributed to the rather large contribution of intercalation to the sodium storage, which is a relatively sluggish process and hardly works at high rates (**Figure 4c**). Therefore, despite its better conductivity, the rate capability is still worse than that of the HAT-CNF-850. The rate capability is to be complemented by the Nyquist plots (**Figure 4e**). All the samples exhibit a semicircle curve in the high frequency region plus a straight line in the low frequency region, which is a typical impedance curve for battery materials. Basically, the diameter of the semicircle represents the interfacial charge transfer resistances, which mainly come from the electric and ionic resistances at the interface between the electrode and the electrolyte in a specific process. The smallest semicircle for HAT-CNF-850 suggests its lowest resistance at favorable processes, leading to the superior rate capability. To summarize, the rate capability depends on the dynamics of the electron and ion transport. The HAT-CNF-700 lacks sufficient electrical conductivity for electron transport, while the HAT-CNF-1000 suffers from the sluggish ion transport dynamics at high rates due to the relatively large portion of intercalation process.

Among these HAT-CNFs, HAT-CNF-850 provides the best overall performance, exhibiting a reversible specific capacity of 361, 269, 149, and 105 mAh g^{-1} at 0.1, 1, 5, and 10 A g^{-1}, respectively. Such a superior capacity and rate capability is attributed to the desirable conductivity, high nitrogen content, fibrous morphology, and high porosity within the fiber surface. The high nitrogen content provides abundant low energy sites for sodium storage, while the graphitic carbon component can accommodate the intercalation of sodium atoms, both giving rise to the capacity. In terms of rate capability, the wide pores of the fibrous structure shortens the transport length of sodium ions, The slow process of intercalation accounts for only a small part of the whole capacity due to the rather low portion of graphitic carbon component. These two factors plus the desirable electrical conductivity

result in its excellent rate capability. The high cycling stability of HAT-CNF-850 is verified by cycling tests, which maintain over 95% of the initial capacity after 500 deep charging-discharging cycles at 0.5 A g^{-1}, indicating sufficient electrochemical stability of our new material throughout cycling (**Figure S5**).

Kinetic analysis of HAT-CNF-850 was further undertaken based on CV curves at different scan rates (**Figure 5**) to separately investigate the contributions of capacitive and diffusion-controlled sodium storage according to the model proposed by Dunn et al.[26] With the increase of the scan rate, the curves maintain similar shapes but the characteristic peaks become broader (**Figure 5a**). Two redox peaks located at 0.12-0.56 V and 1.0-0.5 V are observed, which are supposed to be related to the intercalation and adsorption process, respectively. The relationship between peak current (i) and scan rate (v) is analyzed by the equation $i = av^b$. The value of b = 0.5 indicates a semi-infinite linear diffusion controlled Faradaic process, while b = 1 represents a pseudocapacitive-dominated behavior, i.e., the absence of diffusion limitations. The parameter b can be calculated by the slope of *ln(v)–ln(i)* plots (**Figure 5b**).[27] After linear fitting, the b value of peak 1 is determined to be 0.64, suggesting the diffusion-controlled feature of the slow sodium intercalation process. On the other hand, the b value of peak 2 is calculated to be 0.92, indicating that the chemical adsorption process is mainly dominated by pesudocapacitive behavior. Furthermore, the current response at a fixed potential (U) can be expressed by the equation $i_U = k_1v + k_2v^{1/2}$, considering the contributions from both the pseudocapacitive process (k_1v) and the diffusion-controlled Faradaic process ($k_2v^{1/2}$).[26a] Therefore, the pseudocapacitive and the diffusion-limited contributions at a given potential can be quantified by k_1 and k_2, respectively. Accordingly, 60% of the total capacity at 2 mV s^{-1} is attributed to pseudocapacitive processes, as indicated by the shaded area (**Figure 5c**). The contributions of pseudocapacitive process at different scan rates are also calculated (**Figure 5d**). It can be clearly seen that the pseudocapacitive process contributes more at higher scan rates, indicating the gradually increasing dominance of chemical adsorption process at faster charge/discharge rates.

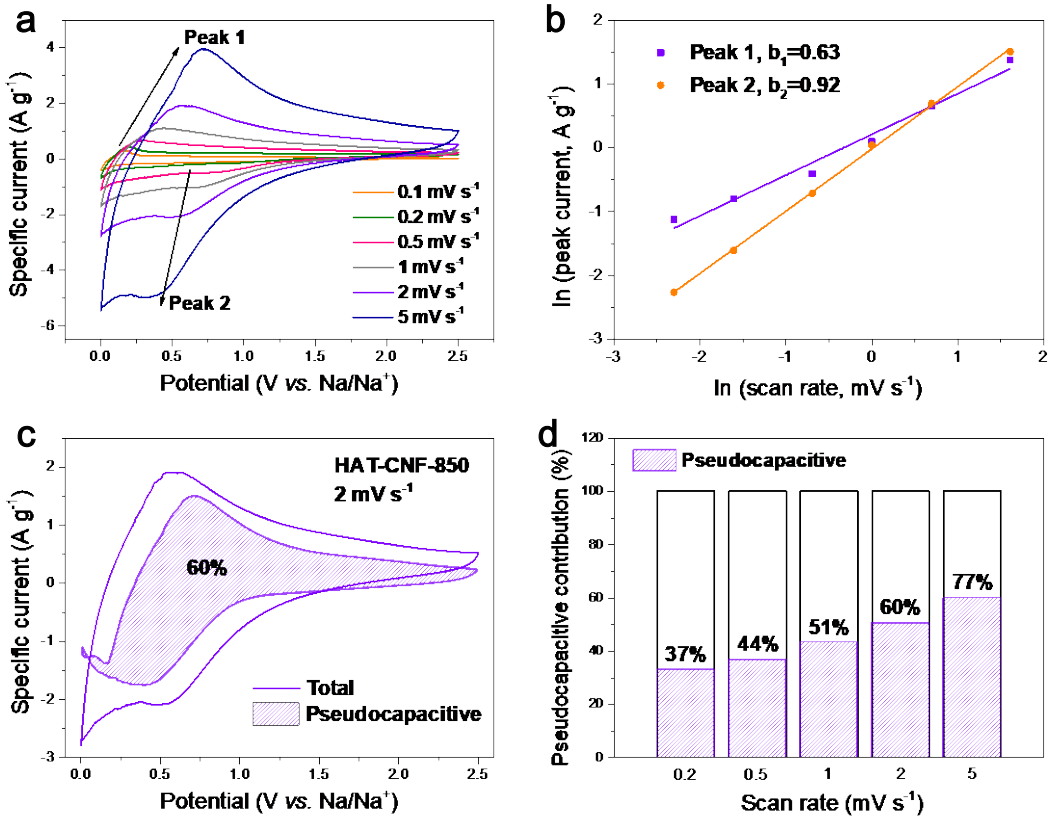

Figure 5. Kinetics analysis of HAT-CNF-850. a) CV curves of HAT-CNF-850 at various sweep rates ranging from 0.1 to 5.0 mV s^{-1}. b) Correlation between the peak current and the scan rate. c) Pseudocapacitive contribution (shaded area) to charge storage at a scan rate of 2 mV s^{-1}. d) Pseudocapacitive contributions of HAT-CNF-850 at various scan rates.

To investigate the influence of the fibrous structure, HAT-CN as such was directly carbonized at 850 °C (HAT-850) with the same procedure of HAT-CNF-850, and employed as electrode material for the half-cell measurements. The nitrogen content of HAT-850 is ~17 wt% as determined by elemental analysis (**Table 1**), thus slightly higher than that of the (also PVP-based) HAT-CNF-850. SEM and TEM images reveal a plate-like morphology of HAT-850 with a particle size of around 10 µm, and the typical disordered microporous structure with a small contribution of mesopores (**Figure 6a-b**). The XRD pattern shows that its local structure is comparable to that of the HAT-CNF-850 (**Figure S6a**). In the N_2 (-196 °C) physisorption experiments, HAT-850 shows a type I(a) isotherm, indicating a porous structure similar to the HAT-CNFs with a slightly higher DFT SSA of 642 m^2 g^{-1} (**Figure S6b**). The increase of the SSA is attributed to the absence of PVP. When employing HAT-

850 as the working electrode for sodium storage, the initial specific discharge and charge capacity is 390 and 168 mAh g^{-1} at 0.1 A g^{-1} (**Figure S6d**), corresponding to an initial Coulombic efficiency of 43%. It provides only a moderate reversible specific capacity of 161 mAh g^{-1} at 0.1 A g^{-1} (**Figure 6c and f**), which 50% less than HAT-CNF-850 (361 mAh g^{-1}) in spite of the higher nitrogen content and higher porosity of HAT-850. Moreover, the intercalation mechanism that significantly contributes to the capacity of HAT-CNF-850 is absent in HAT-850, which is also revealed by the absence of the pronounced peaks at around 0.2 V (**Figure 6d**). HAT-850 also shows relatively inferior rate capability with a specific capacity of 86, 35, and 15 mAh g^{-1} at 1, 5, and 10 A g^{-1}, respectively (**Figure 6c and f**). We attribute all that to the fibrous morphology of the electrospun counterpart, which provides one-dimensional conduction pathways, but also lower lateral dimensions for ion transport perpendicular to the fiber. The superior rate capability of HAT-CNF-850 is also elucidated by the smaller semicircle (lower resistance) in the Nyquist plot (**Figure 6e**).

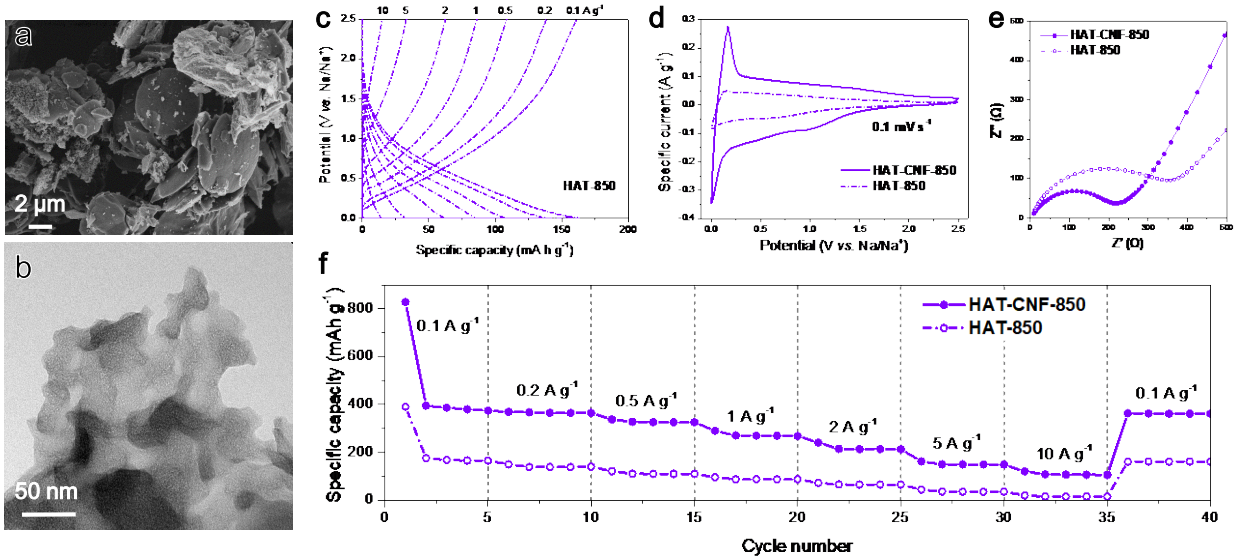

Figure 6. (a) SEM and (b) TEM images of HAT-850. (c) Galvanostatic charge-discharge profiles of HAT-850 at different specific currents. (d) Cyclic voltammetry curves, (e) Nyquist plot, and (f) rate performance of HAT-850 in comparison with those of HAT-CNF-850.

To verify the practical applicability of the electrospun HAT-CNF-based electrodes, a prototype NIC full cell was fabricated with the HAT-CNF-850 and salt-templated carbon (STC-16) as the anode and cathode, respectively. STC-16 with hierarchical micro-mesopore architecture has recently been

identified as an excellent supercapacitor electrode material.[28] It already exhibited good performance as a cathode material in the half-cell NICs with metallic sodium as the counter electrode. The reversible capacity of STC-16 reaches up to 70 mAh g^{-1} at 0.1 A g^{-1} within the voltage range of 3.2 to 4.4 V (**Figure 7a**). The capacity loss in the first cycle can again be attributed to the irreversible side reaction between the carbon surface functional groups and the electrolyte at high cell voltage (4.4 V) and the related high oxidation potentials of + 1.5 V, creating an solid electrolyte interphase layer by reaction with the solvent. Both cathode and anode were activated before assembling the full cell. The anode was cycled for 10 times at 0.1 A g^{-1}, followed by discharging to 0 V to achieve full sodiation. Similarly, the cathode was cycled for 10 times before charging to 4.4 V. The HAT-CNF-850||STC16 full cell was measured with the working voltage cut offs between 0.5 V and 4 V to maximize the utilization of the working potential range of both electrodes and minimizing the risk of electrolyte decomposition or other oxidative side reactions. The nearly rectangular shape of CV curves up to 200 mV s^{-1} (**Figure 7b**), the almost symmetric triangle shape of the galvanostatic charging/discharging curves (**Figure 7c inset**), as well as the practically vertical curves in the low-frequency region of the Nyquist plots (**Figure S7a**) indicate a capacitive-controlled behavior of the NIC. However, slight distortions from the perfect capacitive shape of these curves are likely caused by the non-capacitive intercalation of sodium into the HAT-CNF-850 anode. Calculated by the galvanostatic charging/discharging curves, the specific capacitance of the NIC full cell reaches 55.8 F g^{-1} at a specific current of 0.1 A g^{-1} (according to the total mass of cathode and anode), while it maintains high values of 40, 32, 20, and 15 F g^{-1} at 1, 2, 5, and 10 A g^{-1}, respectively (**Figure 7c**). This is also confirmed by the small voltage drop of 0.54 V even at the high specific current of 10 A g^{-1} (**Figure 7c, inset**). The superior rate capability is attributed to efficient charge carrier transfer, which is also revealed by the Nyquist plot (**Figure S7a**). The small intercept along the real axis (5 Ω) and the minor semicircle illustrate the low intrinsic resistance and high electrical conductivity in both cathode and anode. In the medium frequency region, the 45° sloped curve known as the Warburg portion is related to the transport of

electrolyte ions. The short Warburg lengths indicate good ion transport dynamics and short ion transfer distance, which can be attributed to the 1D fiber structured anode. Accordingly, the Ragone plot (**Figure 7d**) of the NIC shows that the asymmetric cell with the voltage window of 0.5-4.0 V provides the maximum specific energy of 95 Wh kg^{-1} at a specific power of 0.19 kW kg^{-1}, with a slight drop to 65 Wh kg^{-1} at 1.8 kW kg^{-1}, and still maintains 18 Wh kg^{-1} at a specific power of 13 kW kg^{-1}. The specific energy is indeed one order of magnitude higher than that of commercial ECs without losing the excellent power capability. The performance of our HAT-CNF-850||STC16 NIC device can be compared with some recently reported outstanding devices in a Ragone plot (**Figure 7d**). Our metal-free electrodes and non-optimized NIC device exhibit competitive energy/power performance comparable to state-of-the-art NICs, such as such as PI-2.5||AC(PI-5),[29] Na-Ti_3C_2||AC,[30] TiO_2@CNT@C||BAC,[31] $Na_2Ti_2O_4(OH)_2$||RHDPC-KOH,[32] and M-TiO_2-RGO||PDPC.[33] The cycling stability was tested in a cycling test at a specific current of 1 A g^{-1}. After 1000 cycles, a specific capacitance of 34.4 F g^{-1} is maintained corresponding to capacitance retention of 89.9% (**Figure S7b**). The ~10% capacity loss might be related to the large voltage window that causes the degradation in the positive potential range.[34] The Coulombic efficiency is nearly 100% throughout the cycling process, showing the reversibility of the NIC. Thus, this NIC set-up demonstrates a much higher energy density compared to commercial ECs, as well as comparable power density and cycling life, showing great potential as an alternative candidate for future high power electrochemical energy storage.

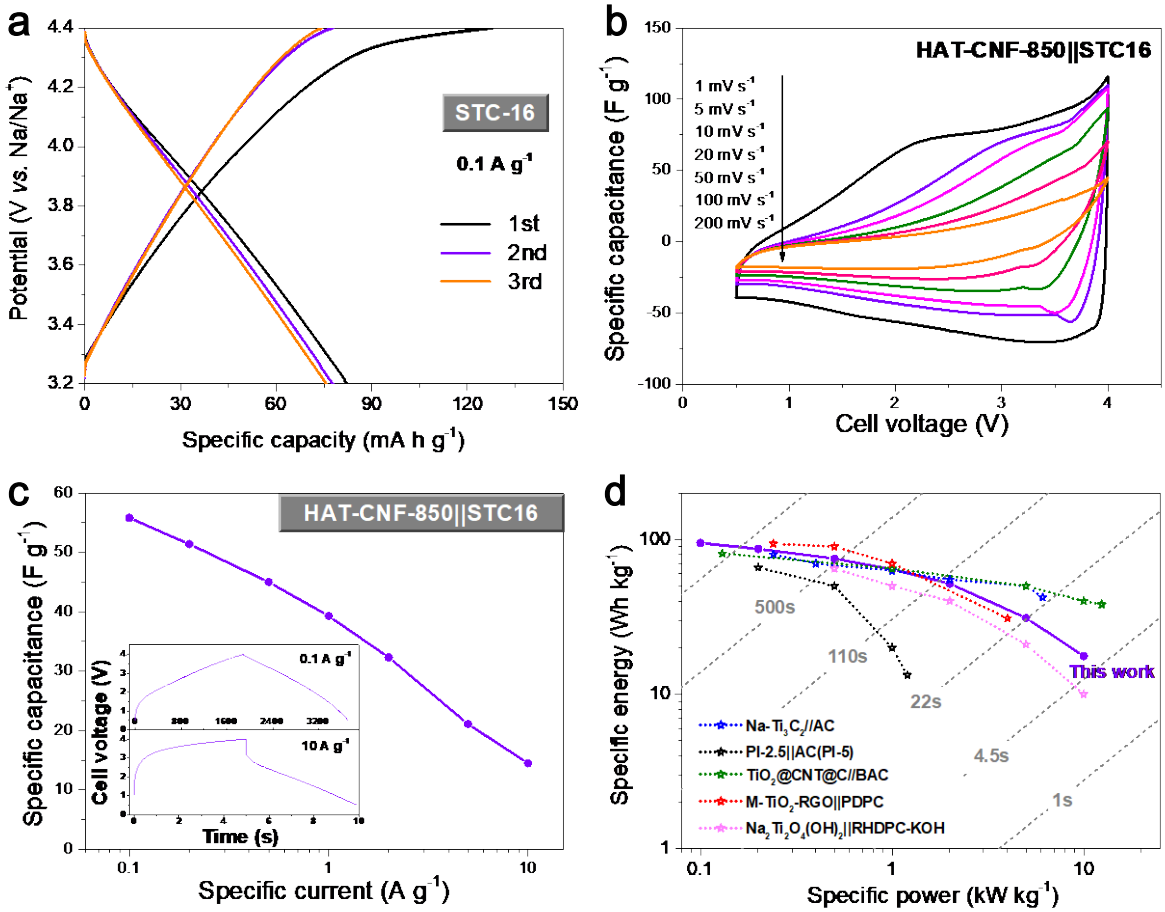

Figure 7. Full-cell test of the NIC with HAT-CNF-850 as anodes and STC-16 as cathodes. (a) Galvanostatic charge-discharge profiles of the initial three cycles of STC-16 at 0.1 A g^{-1} as the cathode in a half cell. (b) Cyclic voltammetry curves (0.5-4.0 V), (c) capacitance retention with specific current increase, and (d) Ragone plots. The inset in (c) represents the galvanostatic charge-discharge profiles of the NIC full cell at 0.1 A g^{-1} and 10 A g^{-1}, respectively.

Conclusion

Free-standing fibrous nitrogen-doped carbon materials (HAT-CNFs) were manufactured by electrospinning of HAT-CN with PVP followed by thermal condensation. The fibers stand out by a high nitrogen content of up to 15 wt%, a well-defined one-dimensional morphology, and microporous nanostructure. The binder-free HAT-CNF-850 electrode delivers a reversible capacity of 361 mAh g^{-1} at 0.1 A g^{-1}. A remarkable capacitance of 106 mAh g^{-1} is retained at the high specific current of 10 A g^{-1}. The material also exhibits excellent stability of 316 mAh g^{-1} at 0.5 A g^{-1} after 500 cycles, corresponding to more than 95% of the initial capacity. The superior capacity and rate capability is

attributed to the high and uniform nitrogen doping introduced by the HAT-CN precursor, as well as the high electrical and ionic conductivity of the 1D interconnected fibrous structure. The abundant nitrogen-containing groups provide active sites for sodium adsorption, which takes place in the high and medium potential range and most significantly contributes to the high capacity. The more graphitic carbon domains at higher condensation temperatures can contribute by the intercalation of sodium in the low potential range below ~0.3 V versus Na/Na^+, a process which is highly dependent on the degree of graphitization and layer distance. Sodium adsorption shows significantly faster dynamics than the intercalation process. Therefore, a possible next step is to further increase the nitrogen content while maintaining the large amounts of available active sites and high electrical conductivity, thus maximizing the ion adsorption capacity to ensure high capacity and good rate capability. The role of the specific chemical architecture of the nitrogen-sites also needs further investigation in order to better understand their contribution to the charge storage.

A full cell device of NIC employing HAT-CNF as the anode and a salt-templated microporous carbon (STC-16) as the cathode provides remarkable energy and power density in the voltage range of 0.5-4.0 V (95 Wh kg^{-1} at 0.19 kW kg^{-1}, and still maintains 18 Wh kg^{-1} at 13 kW kg^{-1}) as well as long cycle life (~90% capacity retention after 1000 cycles). The NIC has the advantages of ECs, while its energy density greatly surpasses that of common ECs. The approach for fabrication of such high nitrogen containing electrodes with desirable electrical conductivity shows great potential to scale up and provides a method to increase the electrochemical performance of anode materials for NICs or sodium-ion batteries.

Experimental Section

Synthesis of hexaazatriphenylene-hexacarbonitrile (HAT-CN): HAT-CN has been synthesized according to a previous procedure.[16] Hexaketocyclohexane octahydrate (4 g, 12.6 mmol) and diaminomaleonitrile (10.88 g, 100.8 mmol) were refluxed in acetic acid (AcOH, 150 mL) for 2 h. The

black suspension was filtered off while hot and washed with hot AcOH (3 × 25 mL) resulting in a black solid. The solid was suspended in 30 % HNO_3 (60 mL) and heated at 100 °C for 3 h. The hot dark brown suspension was poured into ice water (200 mL). The suspension was filtered and the solid was refluxed in acetonitrile (400 mL) for 2 h followed by filtration. The filtrate was evaporated under vacuum yielding an orange solid (2.4 g, yield 50 %).

Synthesis of HAT fiber (HAT-CNF): HAT-CNF-X was fabricated using electrospinning and subsequent condensation. The spinning solution was prepared by stirring HAT-CN (200 mg) and polyvinylpyrrolidone (300 mg) in dimethylformamide (DMF) at 60 °C for 2 h. The solution was loaded to a 2 mL syringe, and mounted on the syringe pump in a spinning machine (Professional Electrospinner, Yflow, Spain). A positive high voltage was connected via alligator clip to a needle with an inner diameter of 0.5 mm and outer diameter of 1 mm. A grounded rotating drum covered with aluminum foil was employed to collect the fibers at a rotation speed of 200 rpm for a duration of 25 min. Process parameters were fixed at a high voltage of 13 kV, flow rate of 2 mL h^{-1} and distance from tip to collector of 15 cm. The temperature was 23°C and the humidity 40-50%. The pristine fibers were then carbonized in a chamber furnace at different temperatures for 1 h under N_2 gas flow. The heating ramp was set up to be 2.5 °C min^{-1} from room temperature to 450 °C, and 4 °C min^{-1} from 450 °C to 700, 850 or 1000 °C. The resulting materials are labelled as HAT-CNF-X, where X stands for the condensation temperature.

Synthesis of salt-templated carbon (STC-16): $ZnCl_2$ was employed as the salt template for the synthesis of STC-16.[28] In a typical process, 30 mL of an aqueous solution of 5 g sucrose, 80 g of $ZnCl_2$ and 0.55 g concentrated sulfuric acid was dried at 100 °C for 6 h, before being heated to 160 °C and kept for 6 h. The mixture was then transferred to a horizontal tubular furnace and heated to 900 °C for 2 h under N_2 flow with heating rate of 1 °C min^{-1}. Then it was thoroughly washed by stirring in 1 M HCl aqueous solution overnight, followed by washing with deionized water and drying at 60 °C for 6 h.

Material characterization: N_2 physisorption experiments were carried out at -196 °C on a Quadrasorb apparatus (40-60 mg sample) from Quantachrome Instruments. Prior to all measurements, the samples were outgassed at 150 °C for 20 h under vacuum. Total pore volumes (V_t) were determined at p/p_0 = 0.95. SSAs and Pore size distributions were calculated using the quenched-solid density functional theory (QSDFT) method (adsorption branch kernel) for N_2 adsorbed on carbon with a slit/cylindrical pore shape at -196 °C from the data obtained by the low-pressure measurements.

Further structural characterization was carried out by transmission electron microscopy (TEM, EM 912 Omega/Carl-Zeiss Oberkochen) operating at 120 kV. To prepare the TEM samples, the carbon material has been dispersed in ethanol by sonication for 10 min, followed by dropping several droplets of the dispersion on a carbon-coated copper TEM grid and drying at room temperature.

Thermogravimetric analysis (TGA) was conducted with a Netzsch TG 209 F1 device under constant N_2 flow in platinum pans at a heating rate of 10 °C min^{-1} to 1000 °C.

Raman spectra were recorded using a Witec Raman Microscope operating at an excitation wavelength of 532 nm with a power of 4.0 mW. After the background noise was subtracted from the obtained Raman spectra, the D, D^2, A, and G bands were fitted with Gaussian functions.

XPS was performed on a Thermo Scientific K-Alpha spectrometer equipped with a monochromatic small-spot X-ray source and a 180° double focusing hemispherical analyzer with a 128-channel delay line detector. Spectra were obtained using an aluminum anode (Al Kα=1486.6eV) operated at 72 W and a spot size of 400 μm. Survey scans were measured at constant pass energy of 200 eV and high-resolution scans of the separate regions were measured at 50 eV pass energy. The background pressure of the ultra-high vacuum (UHV) chamber was $<2\times10^{-8}$ mbar. No special precautions were taken to keep the sample under an inert atmosphere during materials transfer and handling. Sample charging was compensated for by the use of an electron flood gun.

Water vapor physisorption experiments were carried out at 25 °C on an Autosorb IQ instrument from Quantachrome Instruments. Prior to all measurements, the samples were outgassed at 150 °C for 20 h under vacuum.

Electrochemical measurements: The free-standing film of HAT-CNF was punched into free-standing disks of 10 mm in diameter, which were directly used as working electrodes. The areal loading of an electrode was about 0.5 mg cm^{-2}. To prepare the HAT-850 electrode, 80 wt% of the active materials, 10 wt% of carbon black (super-P), 5 wt% of sodium carboxymethyl cellulose (Sigma, average Mw ~250000) and 5 wt% of poly(acrylic acid) (Sigma, average Mw ~450000) were uniformly mixed in Milli-Q water under mechanical stirring. The obtained slurries were transferred onto a copper current collector (10 mm in diameter) and dried at 60 °C overnight. The areal loading of a HAT-850 electrode was about 0.8 mg cm^{-2}. The half-cell tests were carried out using Swagelok-type cells assembled in an argon filled glove box (H_2O < 0.1 ppm, O_2 < 0.1 ppm). Sodium metal (11 mm in diameter) was used as both counter and reference electrodes. Glass fibers (Whatman GF/C, 13 mm in diameter) were employed as the separators. The electrolyte was 1 M $NaClO_4$ in ethylene carbonate/propylene carbonate/fluoroethylene carbonate (45:45:10 by mass). The Swagelok cell was assembled using the working and counter electrodes sandwiching the separator, with 300 µL electrolyte and a copper foil as the current collector for the working electrode. A Biologic MPG-2 galvanostat/potentiostat was used for electrochemical characterization. All measurements were performed at room temperature. The electrochemical impedance spectroscopy was performed at open circuit potential with a sinusoidal signal over a frequency range from 20 kHz to 10^{-2} Hz at an amplitude of 10 mV. Cyclic voltammetry (CV) tests were performed at scan rates of 0.1 mV s^{-1}. Galvanostatic charge/discharge with potential limitation (GCPL) was applied at specific currents between 0.1 and 10 A g^{-1} in a voltage range from 0 to +2.5 V. The specific capacity, Q (mAh g^{-1}), was calculated according to the following equation:

$$Q = \frac{Q_{dis}}{m} \quad (1)$$

Where Q_{dis} (mAh) is the charge of the discharging cycle, and m (g) is the mass of a single HAT-NF electrode.

Full-cell Na-ion capacitors (NICs) were assembled with the HAT-NF-850 as the anode and the STC-16 as the cathode. The preparation method for the cathode was the same as that for the HAT-850 electrode except using the aluminum current collector (10 mm in diameter). The weight ratio between the cathode and anode active materials was set to be 2.5:1. The electrolyte and the separator applied in full cells were all the same as those in half cells. The specific capacitance C (F g^{-1}), specific energy E (Wh kg^{-1}), and specific power P (W kg^{-1}) of NICs were estimated via:

$$C = \frac{Q_{dis}}{(V - V_{drop})M} \tag{2}$$

$$E = \frac{1}{2\times3.6} C(V - V_{drop})^2 \tag{3}$$

$$P = \frac{E\times3600}{\Delta t} \tag{4}$$

where M (g) is total mass of the active materials (cathode and anode), V (V) is the discharging potential change, V_{drop} (V) is the voltage drop at the beginning of the discharge, Δt (s) is the discharging time.

For long-term stability tests, the full cells were charged and discharged by galvanostatic cycling for 1,000 cycles at 1 A g^{-1}.

Acknowledgement. R.Y. and H.H acknowledge financial support from China Scholarship Council. K.L thanks the Research Foundation Flanders (FWO-Vlaanderen) for an International Mobility Grant. Financial support by the Max-Planck Society and ETH Zurich is gratefully acknowledged.

References

[1] a) P. Simon, Y. Gogotsi, *Nat. Mater.* **2008**, *7*, 845; b) G. Wang, L. Zhang, J. Zhang, *Chem. Soc. Rev.* **2012**, *41*, 797; c) M. Salanne, B. Rotenberg, K. Naoi, K. Kaneko, P. L. Taberna, C. P. Grey, B. Dunn, P. Simon, *Nat. Energy* **2016**, *1*, 16070.

[2] P. X. Han, G. J. Xu, X. Q. Han, J. W. Zhao, X. H. Zhou, G. L. Cui, *Adv. Energy Mater.* **2018**, *8*, 1801243.

[3] H. Wang, C. Zhu, D. Chao, Q. Yan, H. J. Fan, *Adv. Mater.* **2017**, *29*, 1702093.

[4] a) A. Eftekhari, *Energy Storage Mater.* **2017**, *9*, 47; b) M. Antonietti, X. Chen, R. Yan, M. Oschatz, *Energy Environ. Sci.* **2018**, *11*, 3069.

[5] a) H. S. Hou, X. Q. Qiu, W. F. Wei, Y. Zhang, X. B. Ji, *Adv. Energy Mater.* **2017**, *7*, 1602898; b) M. S. Balogun, Y. Luo, W. T. Qiu, P. Liu, Y. X. Tong, *Carbon* **2016**, *98*, 162; c) K. Tang, L. J. Fu, R. J. White, L. H. Yu, M. M. Titirici, M. Antonietti, J. Maier, *Adv. Energy Mater.* **2012**, *2*, 873; d) S. Wenzel, T. Hara, J. Janek, P. Adelhelm, *Energy Environ. Sci.* **2011**, *4*, 3342.

[6] Z. Li, J. Ding, D. Mitlin, *Acc. Chem. Res.* **2015**, *48*, 1657.

[7] a) N. Zhang, X. P. Han, Y. C. Liu, X. F. Hu, Q. Zhao, J. Chen, *Adv. Energy Mater.* **2015**, *5*, 1401123; b) E. Lim, C. Jo, M. S. Kim, M.-H. Kim, J. Chun, H. Kim, J. Park, K. C. Roh, K. Kang, S. Yoon, J. Lee, *Adv. Funct. Mater.* **2016**, *26*, 3711.

[8] a) P. B. Geng, S. S. Zheng, H. Tang, R. M. Zhu, L. Zhang, S. Cao, H. G. Xue, H. Pang, *Adv. Energy Mater.* **2018**, *8*, 1703259; b) Z. Hu, Q. N. Liu, S. L. Chou, S. X. Dou, *Adv. Mater.* **2017**, *29*, 1700606; c) Y. Xiao, S. H. Lee, Y. K. Sun, *Adv. Energy Mater.* **2017**, *7*, 1601329.

[9] X. W. Zhong, Y. Wu, S. F. Zeng, Y. Yu, *Chem-Asian J* **2018**, *13*, 1248.

[10] a) F. Li, Z. Zhou, *Small* **2018**, *14*; b) L. Shi, T. S. Zhao, *J. Mater. Chem. A* **2017**, *5*, 3735; c) P. Lu, Y. Sun, H. Xiang, X. Liang, Y. Yu, *Adv. Energy Mater.* **2018**, *8*, 1702434.

[11] a) J. W. Jung, C. L. Lee, S. Yu, I. D. Kim, *J. Mater. Chem. A* **2016**, *4*, 703; b) H. G. Wang, S. Yuan, D. L. Ma, X. B. Zhang, J. M. Yan, *Energy Environ. Sci.* **2015**, *8*, 1660.

[12] S. Wang, L. Xia, L. Yu, L. Zhang, H. Wang, X. W. D. Lou, *Adv. Energy Mater.* **2016**, *6*, 1502217.

[13] a) J. T. Xu, M. Wang, N. P. Wickramaratne, M. Jaroniec, S. X. Dou, L. M. Dai, *Adv. Mater.* **2015**, *27*, 2042; b) K. F. Huo, W. L. An, J. J. Fu, B. Gao, L. Wang, X. Peng, G. J. Cheng, P. K. Chu, *J. Power Sources* **2016**, *324*, 233; c) Z. G. Wang, Y. M. Li, X. J. Lv, *Rsc Adv* **2014**, *4*, 62673.

[14] J. T. Xu, J. Mahmood, Y. H. Dou, S. X. Dou, F. Li, L. M. Dai, J. B. Baek, *Adv. Mater.* **2017**, *29*, 1702007.

[15] a) D. A. Stevens, J. R. Dahn, *J. Electrochem. Soc.* **2001**, *148*, A803; b) B. A. Zhang, C. M. Ghimbeu, C. Laberty, C. Vix-Guterl, J. M. Tarascon, *Adv. Energy Mater.* **2016**, *6*, 1501588; c) D. A. Stevens, J. R. Dahn, *J. Electrochem. Soc.* **2000**, *147*, 1271; d) Y. L. Cao, L. F. Xiao, M. L. Sushko, W. Wang, B. Schwenzer, J. Xiao, Z. M. Nie, L. V. Saraf, Z. G. Yang, J. Liu, *Nano Lett.* **2012**, *12*, 3783; e) J. Ding, H. L. Wang, Z. Li, A. Kohandehghan, K. Cui, Z. W. Xu, B. Zahiri, X. H. Tan, E. M. Lotfabad, B. C. Olsen, D. Mitlin, *ACS Nano* **2013**, *7*, 11004; f) C. Bommier, T. W. Surta, M. Dolgos, X. L. Ji, *Nano Lett.* **2015**, *15*, 5888.

[16] a) J. T. Rademacher, K. Kanakarajan, A. W. Czarnik, *Synthesis-Stuttgart* **1994**, 378; b) B. Kurpil, A. Savateev, V. Papaefthimiou, S. Zafeiratos, T. Heil, S. Ozenler, D. Dontsova, M. Antonietti, *Appl Catal B-Environ* **2017**, *217*, 622; c) R. Walczak, B. Kurpil, A. Savateev, T. Heil, J. Schmidt, Q. Qin, M. Antonietti, M. Oschatz, *Angew Chem Int Edit* **2018**, *57*, 10765.

[17] M. Thommes, K. Kaneko, A. V. Neimark, J. P. Olivier, F. Rodriguez-Reinoso, J. Rouquerol, K. S. W. Sing, *Pure Appl. Chem.* **2015**, *87*, 1051.

[18] A. V. Neimark, Y. Z. Lin, P. I. Ravikovitch, M. Thommes, *Carbon* **2009**, *47*, 1617.

[19] K. Faber, F. Badaczewski, M. Oschatz, G. Mondin, W. Nickel, S. Kaskel, B. M. Smarsly, *J. Phys. Chem. C* **2014**, *118*, 15705.

[20] M. Oschatz, P. Pre, S. Dorfler, W. Nickel, P. Beaunier, J. N. Rouzaud, C. Fischer, E. Brunner, S. Kaskel, *Carbon* **2016**, *105*, 314.
[21] a) M. L. Zhao, Y. Cao, X. Q. Liu, J. H. Deng, D. J. Li, H. Q. Gu, *Nanoscale Res Lett* **2014**, *9*; b) J. M. Stillahn, K. J. Trevino, E. R. Fisher, *ACS Appl. Mater. Interfaces* **2011**, *3*, 1402.
[22] J. Zhong, J. J. Deng, B. H. Mao, T. Xie, X. H. Sun, Z. G. Mou, C. H. Hong, P. Yang, S. D. Wang, *Carbon* **2012**, *50*, 335.
[23] H. Huang, D. Kundu, R. Yan, E. Tervoort, X. Chen, L. Pan, M. Oschatz, M. Antonietti, M. Niederberger, *Adv. Energy Mater.* **2018**, 1802800.
[24] a) Z. H. Tian, N. Fechler, M. Oschatz, T. Heil, J. Schmidt, S. G. Yuan, M. Antonietti, *J. Mater. Chem. A* **2018**, *6*, 19013; b) M. Oschatz, M. Antonietti, *Energy Environ. Sci.* **2018**, *11*, 57.
[25] G. P. Hao, G. Mondin, Z. K. Zheng, T. Biemelt, S. Klosz, R. Schubel, A. Eychmuller, S. Kaskel, *Angew Chem Int Edit* **2015**, *54*, 1941.
[26] a) J. Wang, J. Polleux, J. Lim, B. Dunn, *J. Phys. Chem. C* **2007**, *111*, 14925; b) T. Brezesinski, J. Wang, S. H. Tolbert, B. Dunn, *Nat. Mater.* **2010**, *9*, 146; c) J. Yang, Z. Ju, Y. Jiang, Z. Xing, B. Xi, J. Feng, S. Xiong, *Adv. Mater.* **2018**, *30*, 1700104; d) D. Li, L. Zhang, H. Chen, J. Wang, L.-X. Ding, S. Wang, P. J. Ashman, H. Wang, *J. Mater. Chem. A* **2016**, *4*, 8630.
[27] a) H. J. Huang, D. Kundu, R. Y. Yan, E. Tervoort, X. Chen, L. Pan, M. Oschatz, M. Antonietti, M. Niederberger, *Adv. Energy Mater.* **2018**, *8*; b) Q. L. Wei, Y. L. Jiang, X. S. Qian, L. Zhang, Q. D. Li, S. S. Tan, K. N. Zhao, W. Yang, Q. Y. An, J. H. Guo, L. Q. Mai, *Iscience* **2018**, *6*, 212.
[28] R. Y. Yan, M. Antonietti, M. Oschatz, *Adv. Energy Mater.* **2018**, *8*, 1800026.
[29] Q. L. Zhao, D. F. Yang, A. K. Whittaker, X. S. Zhao, *J. Power Sources* **2018**, *396*, 12.
[30] J. M. Luo, C. Fang, C. B. Jin, H. D. Yuan, O. W. Sheng, R. Y. Fang, W. K. Zhang, H. Huang, Y. P. Gan, Y. Xia, C. Liang, J. Zhang, W. Y. Li, X. Y. Tao, *J. Mater. Chem. A* **2018**, *6*, 7794.
[31] Y. E. Zhu, L. P. Yang, J. Sheng, Y. N. Chen, H. C. Gu, J. P. Wei, Z. Zhou, *Adv. Energy Mater.* **2017**, *7*, 1701222.
[32] B. Babu, M. M. Shaijumon, *J. Power Sources* **2017**, *353*, 85.
[33] R. T. Wang, S. J. Wang, Y. B. Zhang, D. D. Jin, X. Y. Tao, L. Zhang, *J. Mater. Chem. A* **2018**, *6*, 1017.
[34] J. Ding, H. Wang, Z. Li, K. Cui, D. Karpuzov, X. Tan, A. Kohandehghan, D. Mitlin, *Energy Environ. Sci.* **2015**, *8*, 941.